RSC Advances

ROYAL SOCIETY OF CHEMISTRY

www.rsc.org/advances

Journal Name

Dynamic Article Links ►

Cite this: DOI: 10.1039/c0xx00000x
www.rsc.org/xxxxxx

ARTICLE TYPE

Self-assembled graphene-constructed hollow Fe_2O_3 spheres with controllable size for high lithium storage

Yanwei Chen[a], Jinzuan Wang[a], Jianzhong Jiang[a], Ming'an Zhou[a], Jun Zhu[a], Sheng Han[a]*

ABSTRACT:

Graphene-constructed hollow Fe_2O_3 spheres (GHFs) were prepared by a one-pot hydrothermal process. The Fe_2O_3 particles were perfectly constructed using graphene sheets. This strategy was an easy method for the large-scale synthesis of GHFs. The size of Fe_2O_3 spheres ranged from 2000 nm to 50 nm and can be easily controlled by changing the weight ratio of GO to $FeCl_2$, and the size greater than 250 nm shows a hollow structure obviously. As the anode material for lithium-ion batteries, the GHFs (300 nm) showed an excellent reversible capacity of 950 mA h g^{-1} after 50 cycles at a charge–discharge rate of 100 mA g^{-1}, and delivered a reversible capacity as high as 640 mA h g^{-1} at a high rate of 1000 mA g^{-1}. The outstanding electrochemical performance of GHFs can be attributed to the graphene-constructed hollow Fe_2O_3 spheres and the synergistic interaction between uniformly dispersed Fe_2O_3 particles and graphene. Moreover, the favorable performance of GHFs can be attributed to the reduced diffusion length of lithium, in which the hollow structure of Fe_2O_3 spheres played an important role.

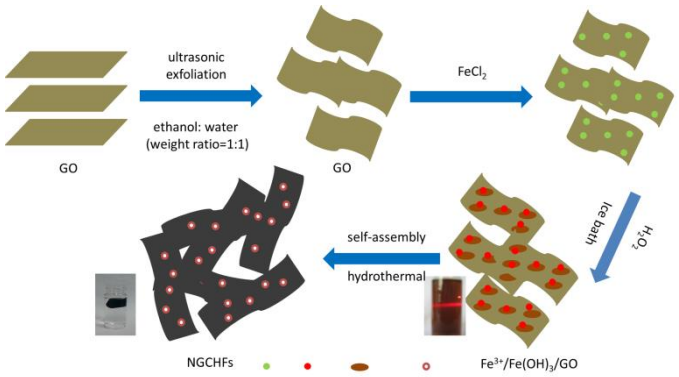

KEYWORDS: hollow Fe_2O_3 spheres, self-assembly, anode material, lithium-ion batteries

1. INTRODUCTION

Lithium-ion batteries (LIBs) are some of the most promising types of batteries because of their high energy density, low maintenance, and relatively low self-discharge.[1-3] In classical commercial LIBs, graphitic carbon is the most commonly used anode material. Development of new electrode materials with high energy densities has been one of the most important pursuits to satisfy the ever-growing demand for high performance LIBs.[4-6] Nanostructured metal oxides, (MOs) such as SnO_2[7, 8], TiO_2[9], Co_3O_4[10, 11], MnO_2[12-14], Mn_3O_4[15], Fe_3O_4[16], and Fe_2O_3[17], are regarded as potential anode materials for LIBs because of their high reversible capacity, high power capability, safety, and long cycle life. Among them, Fe_2O_3 has attracted considerable attention, owing to its high theoretical specific capacity (1005 mA h g^{-1}), low cost, and is environmentally-safe.[18-20] However, low conductivity and pulverization problem, which can cause a breakdown in electrical contact pathways between MO particles, lead to rapid capacity fading during charge–discharge cycling.[17, 21, 22] To address these problems, conducting carbon matrices were used to buffer volume changes and improve structural stability of electrodes.[23-25]

Graphene, a honeycomb network of sp^2 carbon lattices, has been considered as one of the most appealing carbon matrices for MO particles because of outstanding charge carrier mobility and mechanical robustness.[26, 27] Nevertheless, to the best of our knowledge, Fe_2O_3 usually grows on the surface of graphene in other works,[21, 28, 29] and hollow structure is usually fabricated with template,[30-32] a study on graphene-constructed hollow Fe_2O_3 spheres with size-controlled synthesis has not been reported up to date. Therefore, developing size-controlled graphene-constructed G/MO hybrids that can address aggregation of nanoparticles is highly desirable.

In this work, a novel class of GHFs was fabricated by a one-pot hydrothermal method and freeze-drying process. Fe_2O_3 particles, with uniform dispersion and similar sizes, were synthesized by a hydrothermal procedure using $FeCl_2$ and graphene oxide (GO) as precursors. The overall synthesis procedure of GHFs is illustrated in Scheme 1. Compared with the Fe_2O_3 particles supported on graphene sheets, GHFs are perfectly constructed with uniform dispersion. Furthermore, GHFs were size-controlled and provided highly conductive networks with increased surface areas and short diffusion path lengths for lithium ion transport. As a result, GHFs exhibited outstanding reversible capacity and excellent rate performance (950 mA h g^{-1} after 50 cycles at a charge–discharge rate of 100 mA g^{-1} and reversible capacity 640 mA h g^{-1} at a high rate of 1000 mA g^{-1}), when used as the anode material for lithium storage.

2. EXPERIMENTAL SECTION

2.1. Materials. Graphite flakes, $NaNO_3$, $KMnO_4$, 98%H_2SO_4, 30%H_2O_2, $FeCl_2{\cdot}4H_2O$, 37%HCl, iron powder, and ethanol were purchased from Sinopharm Chemical Reagent Co. Ltd. (Shanghai, China). All chemicals, except $FeCl_2{\cdot}4H_2O$, were of analytical grade.

$FeCl_2$ solution, 0.2 M (freshly-prepared).

2.2. Synthesis of HCHFs. GO was synthesized from natural graphite flakes using a modified Hummers method. Exfoliation was carried out by ultrasonication of the GO dispersion under ambient conditions. $FeCl_2$ (0.2 g ml^{-1}) was synthesized from $FeCl_2{\cdot}4H_2O$ as follows. $FeCl_2{\cdot}4H_2O$ (15.7 g) was dissolved in distilled water to a volume of 100 cm^3. For the preparation of GHFs, 60 ml of 2.5 mg ml^{-1} GO suspension was added to 30 g ethanol, and ultrasonicated for 10 min. $FeCl_2$ (0.5 ml 0.2 g ml^{-1}) was added to 10 g ethanol. GO was added fast to the $FeCl_2$-ethanol mixture, then 3 ml H_2O_2 (wt. % = 30) was added slowly with vigorous stirring, and then ultrasonicated for 10 min at room temperature. The resulting suspension was sealed in a 200 ml Teflon-lined autoclave and hydrothermally treated at 180 ℃ for 10 h. The prepared sample was on dialysis for 7 days, and freeze-dried overnight. For comparison purposes, different volumes of $FeCl_2$, ranging from 0.2 ml to 3 ml, were used. Bare Fe_2O_3

particles were also synthesized without GO addition.

2.3. Characterization of Materials. Morphology of the samples was investigated with a field-emission scanning electron microscopy (FESEM) system (FEI, Sirion 200). Materials were characterized by power X-ray diffraction (XRD) using a Rigaku X-ray diffractometer with Cu-Kα irradiation (λ = 0.15406 nm) at 40 kV, 20 mA over the 2θ range from 10 °to 70 °. Thermogravimetric analysis (TGA) was employed by a TA Q5000IR with a heating rate of 10 ℃ min^{-1} under flowing air. Nitrogen adsorption/desorption isotherms at 77 K were determined by Micrometrics SAP 2010.

2.4. Electrochemical Measurements. Electrochemical properties of the samples were evaluated with CR 2010 coin cells. Test electrodes were prepared by mixing active materials with conductive carbon black (super P) as the conductive agent and polyvinylidene fluoride (PVDF) dissolved in N-methyl-2-pyrrolidone (NMP) as the binder in a weight ratio of 80:10:10 to form a slurry, which was then coated onto a copper foil. The mass of active material on each anode was 1.0 mg. Pure lithium foil was used as counter electrodes. Celgard 2400 microporous polypropylene membrane was used as a separator. The electrolyte consisted of a solution of 1 M $LiPF_6$ in ethylene carbonate-dimethyl carbonate-diethyl carbonate (1:1:1 weight ratio). CR 2016 coin cells were assembled in an argon-filled glovebox with water and oxygen content less than 1 ppm. Discharge and charge measurement was carried out with a LAND 2001A system with cutoff potentials 0.01 V for discharge and 3.0 V for charge.

3. RESULTS AND DISCUSSION

The synthesis route to GHFs is illustrated in Scheme 1. First, Fe^{2+} cations from $FeCl_2$ bind with oxygen-containing groups on GO sheets through electrostatic interactions. Second, $Fe(OH)_3$ was freshly synthesized after addition of H_2O_2. In this process, $Fe(OH)_3$ and GO hydrogels were dispersed homogeneously. Third, Fe_2O_3 transformed from $Fe(OH)_3$ hydrogel was constructed by GO and self-assembled, forming a hollow sphere by hydrothermal treatment. GO is simultaneously transformed into RGO. Finally, dark grey GHFs are obtained after dialysis and freeze-drying.

Scheme 1. Schematic of the Synthesis Route to GHFs

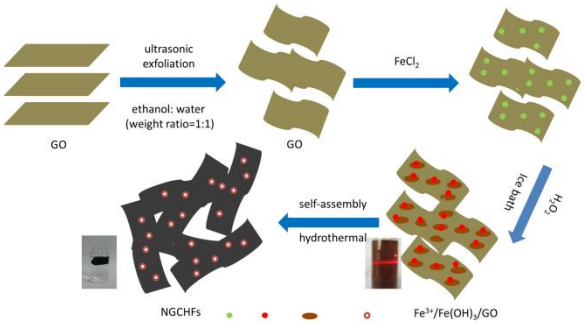

The morphology and microstructure of the synthesized GHFs were elucidated by means of FESEM and nitrogen adsorption/desorption analysis. FESEM images of cross-sections of GHFs (Figure 1) clearly show Fe_2O_3 particles (greater than 200 nm) with a hollow structure and almost all particles were perfectly covered with graphene. The encapsulated graphene sheet can efficiently prevent aggregation of particles and prevent direct contact between Fe_2O_3 particles and the electrolyte. Results reveal that graphene is a notably thin, well-defined, and interconnected network. Geometric confinement of MO particles within graphene layers were reported to enhance interface contact and suppress dissolution and agglomeration of particles, thereby promoting electrochemical activity and stability of the composites. Fe_2O_3 particles ranked randomly, so some hollow structure will be covered, more photos was attached in Figure S4.

A possible hypothesis of the hollow Fe_2O_3 sphere: First, in a typical process, GO should be salted out while $FeCl_2$ was added, but in this experiment, $FeCl_3$ and $Fe(OH)_3$ generated after H_2O_2 was added into the mixture under 0 ℃, in this process, the water distributed in the mixture will be redistributed, and GO salted out will be redistributed into the water since $Fe(OH)_3$ should contain a large amount of H_2O, then a homogeneous solution with $FeCl_3$, $Fe(OH)_3$, GO , water and C_2H_5OH generated.(Figure S5)

When the mixture was hydrothermally treated at 180 ℃, $Fe(OH)_3$ close to GO loss the contained water fast and gather together as GO was a good thermal conductive material, in this process, graphene is also gather outside and greatly prevent the $Fe(OH)_3$ from gathering fast, until Fe_2O_3 was gather to generated a hard shell, $Fe(OH)_3$ covered inside will gather to the shell with graphene

constructed, then, a hollow Fe_2O_3 sphere generated.

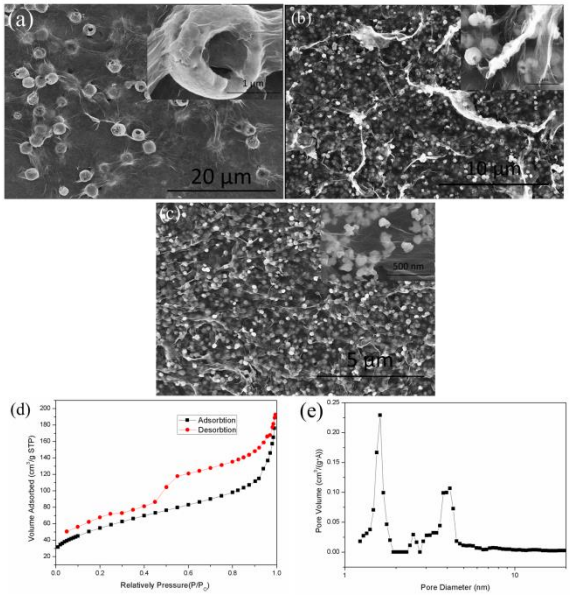

Figure 1. (a–c) Typical FESEM image of GHFs revealing graphene-constructed structure and Fe_2O_3 particle diameter of 2000, 300, and 100 nm. (d, e) Nitrogen adsorption/desorption isotherms and pore size distribution of Fe_2O_3/GAs.

Brunauer–Emmmett–Teller analysis of nitrogen adsorption/desorption isotherms reveal that specific surface area of GHFs (Fe_2O_3 particle diameter of 300 nm) was 201 m^2 g^{-1}, which was much higher than that of bare Fe_2O_3. The pore volume was 0.244 cm^3 g^{-1} for GHFs. Moreover, the majority of pore sizes calculated by the Barret–Joyner–Halenda method are 1.6, 2.5, and 4 nm.

TGA measurement carried out in the air was used to determine the chemical composition of GHFs (Fe_2O_3 particle diameter of 300 nm). In Figure 2a, the TGA curve displays a significant weight loss at approximately 450 ℃ and a constant weight above 500 ℃. The minimal weight loss below 300 ℃ was probably caused by the evaporation of adsorbed water molecules. The major weight loss from 300 ℃ to 500 ℃ was approximately 20%, which indicates combustion of graphene. On the basis of calculations, Fe_2O_3 content of in GHFs was 78%. Crystalline structure of the final products was determined by XRD. XRD pattern of GHFs corresponds to the upper profile in Figure 2b, and all the peaks can be attributed to Fe_2O_3 (JCPDS No, 33-0664). At 26 °, an apparent diffraction peak corresponding to graphene was not observed in the XRD pattern of GHFs, which indicate the graphene in GHFs is dispersed uniformly without packed. The XRD pattern of the burned sample was pure Fe_2O_3 and date was attached in the Figure S3, and all the peaks can be attributed to Fe_2O_3 (JCPDS No, 33-0664).

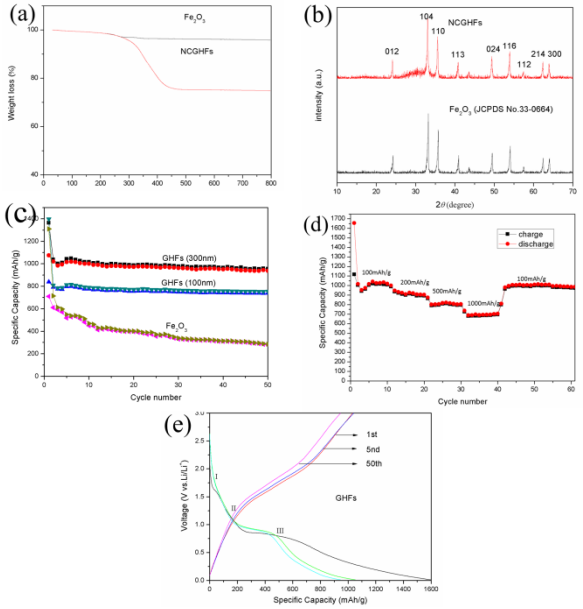

Figure 2. (a) TGA curves for Fe_2O_3 particles and GHFs in the air. (b) XRD patterns of GHFs and Fe_2O_3. (c) Cycling performance of GHFs (300nm and 100nm) and Fe_2O_3 at the current density of 100 mAg−1. (d) Rate capacity of GHFs between 0.01 and 3.0 V with increasing current density. (e) Discharge/charge profiles of GHFs. Diameter of Fe_2O_3 particles in all GHFs is 300 nm

Galvanostatic discharge (Li insertion)-charge (Li extraction) measurements were carried out at a current density of 100 mA g^{-1} over a voltage range from 0.01–3.0 V to evaluate the electrochemical performance of the as-prepared GHFs. The first lithium insertion profile can be divided into three stages, namely, Fe_2O_3-Li_x, Fe_2O_3-cubic, and $Li_2Fe_2O_3$-Fe+Li_2O. At the early stage of lithium insertion (plateau I), a minimal amount of lithium was inserted into the crystalline structure of Fe_2O_3 before hexagonal to cubic stacking structural transformation of the close-packed anionic array. In the stage of lithium insertion (plateau II), a profile similar with plateau I was found, and a long plateau III appeared at approximately 0.8 V, corresponding to a reversible reaction between cubic $Li_2Fe_2O_3$ and Fe in the third stage.[33-35] The first discharge–charge step of GHFs (300 nm) delivered a specific discharge capacity of 1353 mA

h g^{-1} and charge capacity of 1120 mA h g^{-1}, with initial Coulombic efficiency of 82.1%. T The first discharge–charge step of GHFs (100 nm) delivered a specific discharge capacity of 1382 mA h g^{-1} and charge capacity of 831 mA h g^{-1}, with initial Coulombic efficiency of 60.1% and Coulombic efficiencies were close to 98%. Typically, when the electrode size down to a certain point, the electrode pulverization can be effectively relieved, therefore facilitating the formation of a stable SEI. And the SEI formed in the lithiated expanded state can be broken as the nanostructure shrinks during delithiation.[36] In our materials, Fe_2O_3 was constructed by graphene, so the electrode pulverization can be effectively relieved, while the SEI could also be relieved by the stable structure and property of graphene. A direct comparison with Fe_2O_3 shows the synergistic effect between Fe_2O_3 and RGO. Fe_2O_3 without RGO covered delivered a specific discharge capacity of 1320mA h g^{-1}, but a charge capacity of 710 mA h g^{-1} (Figure 3c). This initial capacity loss could be attributed to the formation of a solid electrolyte interphase (SEI) layer on the electrode surface during the first discharge step. At the end of 50 charge–discharge cycles, a reversible capacity as high as 950 mA h g^{-1} of GHFs (300 nm) and 790 mA h g^{-1} of GHFs (100 nm) can be retained, which was much higher than the theoretical specific capacity of graphene (372 mA h g^{-1}). The rate performances of GHFs at current rates of 100–1000 mA g^{-1} are depicted in Figure 3d. Reversible capacities were retained at 890 and 774 mA h g^{-1} at 200 and 500 mA g^{-1}, and Coulombic efficiencies were close to 98%. Remarkably, a reversible capacity of 640 mA h g^{-1} can be delivered at a very high rate of 1000 mA g^{-1}. The prominent difference between GHFs and Fe_2O_3 emphasizes the efficiency of our protocol in the improvement of the electrochemical performance of Fe_2O_3 by incorporation with graphene. Moreover, performance stability of GHFs at high rates indicates ultrafast diffusion of lithium ions in bulk because of the short diffusion path length and stable graphene structure.

Thus, graphene architecture in GHFs not only improved the conductivity of the overall electrode, but also enhanced the electrochemical activity during the cycling process.

The high capacity, favorable cycling stability, and excellent rate capability of GHFs can be attributed to synergistic interactions between Fe_2O_3 particles and graphene associated with an interconnected macroporous framework. First, the graphene networks and the hollow Fe_2O_3 spheres provide a large surface area (201 m^2 g^{-1}) and efficiently reduce diffusion length for both electrons and lithium ions. Second, conductive graphene can serve as multidimensional pathways to facilitate transport of electrons in the bulk electrode. Finally, majority of Fe_2O_3 particles were encapsulated within the graphene sheets, which can suppress the aggregation of Fe_2O_3 particles to allow volume expansion during cycling.

4. CONCLUSIONS

In summary, monolithic GHFs were successfully fabricated by a one-pot hydrothermal reaction and subsequent freeze-drying process. Compared with the Fe_2O_3 particles supported on graphene sheets, GHFs are perfectly constructed with uniform dispersion. Furthermore, Fe_2O_3 particles were size-controlled and hollow. GHFs (300 nm) were applied as LIBs anodes and demonstrated superb enhancement of durability and rate performance with a very high reversible capacity of 950 mA h g^{-1} at a rate of 100 mA g^{-1}, even after 50 cycles, 640 mA h g^{-1} at a high rate of 1000 mA g^{-1}. Our present synthesis strategy could be further extended to the development of other graphene-based MO monoliths as high performance electrode materials with high specific capacities and rate capabilities in LIBs.

AUTHOR INFORMATION

Corresponding Author

*E-mail: hansheng654321@sina.com.

Address: Shanghai Institute of Technology, Shanghai 200235, China.

Fax: + 86-012-60877231

Notes

The authors declare no competing financial interest.

ACKNOWLEDGMENTS

This project was supported by the Innovation Program of Shanghai Municipal Education Commission (Project Number 09YZ387), Innovation Program of Shanghai Municipal Education Commission (Project Number 11ZZ179), Science and Technology Commission of Shanghai Municipality (Project Number 09QT1400600), ShuGuang Project(Project Number 11SG54), National Natural Science Foundation of China (Project Number 20976105) and Shanghai Leading Academic Discipline Project (Project Number J51503).

NOTE AND REFERENCES

[a]*School of Chemical and Environmental Engineering, Shanghai Institute of Technology, Shanghai 201418, China. E-mail: hansheng654321@sina.com*

1. Luo, B.; Liu, S.; Zhi, L. *Small* **2012,** 8, (5), 630-646.

2. Liu, D.; Cao, G. *Energy & Environmental Science* **2010,** 3, (9), 1218-1237.

3. Bruce, P. G.; Scrosati, B.; Tarascon, J. M. *Angewandte Chemie International Edition* **2008,** 47, (16), 2930-2946.

4. Maier, J. *Nature materials* **2005,** 4, (11), 805-815.

5. Aricò, A. S.; Bruce, P.; Scrosati, B.; Tarascon, J.-M.; Van Schalkwijk, W. *Nature materials* **2005,** 4, (5), 366-377.

6. Idota, Y.; Kubota, T.; Matsufuji, A.; Maekawa, Y.; Miyasaka, T. *Science* **1997,** 276, (5317), 1395-1397.

7. Wang, Z.; Luan, D.; Boey, F. Y. C.; Lou, X. W. *Journal of the American Chemical Society* **2011,** 133, (13), 4738-4741.

8. Wang, C.; Zhou, Y.; Ge, M.; Xu, X.; Zhang, Z.; Jiang, J. *Journal of the American Chemical Society* **2009,** 132, (1), 46-47.

9. Yang, S.; Feng, X.; Müllen, K. *Advanced Materials* **2011,** 23, (31), 3575-3579.

10. Yang, S.; Feng, X.; Ivanovici, S.; Müllen, K. *Angewandte Chemie International Edition* **2010,** 49, (45), 8408-8411.

11. Yang, S.; Feng, X.; Wang, L.; Tang, K.; Maier, J.; Müllen, K. *Angewandte Chemie International Edition* **2010,** 49, (28), 4795-4799.

12. Gu, X.; Chen, L.; Ju, Z.; Xu, H.; Yang, J.; Qian, Y. *Advanced Functional Materials* **2013,** 23, (32), 4049-4056.

13. Li, L.; Raji, A. R. O.; Tour, J. M. *Advanced Materials* **2013,** 25, (43), 6298-6302.

14. Guo, C. X.; Wang, M.; Chen, T.; Lou, X. W.; Li, C. M. *Advanced Energy Materials* **2011,** 1, (5), 736-741.

15. Wang, H.; Cui, L.-F.; Yang, Y.; Sanchez Casalongue, H.; Robinson, J. T.; Liang, Y.; Cui, Y.; Dai, H. *Journal of the American Chemical Society* **2010,** 132, (40), 13978-13980.

16. Qu, Q.; Yang, S.; Feng, X. *Advanced Materials* **2011,** 23, (46), 5574-5580.

17. Zhu, X.; Zhu, Y.; Murali, S.; Stoller, M. D.; Ruoff, R. S. *Acs Nano* **2011,** 5, (4), 3333-3338.

18. Jang, B.; Park, M.; Chae, O. B.; Park, S.; Kim, Y.; Oh, S. M.; Piao, Y.; Hyeon, T. *Journal of the American Chemical Society* **2012,** 134, (36), 15010-15015.

19. Xin, J.; Jia-jia, C.; Jian-hui, X.; Yi-ning, S.; You-zuo, F.; Min-sen, Z.; Quan-feng, D. *Chem. Commun.* **2012,** 48, (59), 7410-7412.

20. Wang, B.; Chen, J. S.; Wu, H. B.; Wang, Z.; Lou, X. W. *Journal of the American Chemical Society* **2011,** 133, (43), 17146-17148.

21. Zou, Y.; Kan, J.; Wang, Y. *The Journal of Physical Chemistry C* **2011,** 115, (42), 20747-20753.

22. Zhu, J.; Lu, Z.; Oo, M. O.; Hng, H. H.; Ma, J.; Zhang, H.; Yan, Q. *Journal of Materials Chemistry* **2011,** 21, (34), 12770-12776.

23. Li, Q.; Zhang, S.; Dai, L.; Li, L.-s. *Journal of the American Chemical Society* **2012,** 134, (46), 18932-18935.

24. Yang, L.; Liu, L.; Zhu, Y.; Wang, X.; Wu, Y. *Journal of Materials Chemistry* **2012,** 22, (26), 13148-13152.

25. Su, Y.; Li, S.; Wu, D.; Zhang, F.; Liang, H.; Gao, P.; Cheng, C.; Feng, X. *Acs Nano* **2012,** 6, (9), 8349-8356.

26. Wu, D.; Zhang, F.; Liang, H.; Feng, X. *Chemical Society Reviews* **2012,** 41, (18), 6160-6177.

27. Wu, D.; Zhang, F.; Liu, P.; Feng, X. *Chemistry-A European Journal* **2011,** 17, (39), 10804-10812.

28. Xue, X.-Y.; Ma, C.-H.; Cui, C.-X.; Xing, L.-L. *Solid*

State Sciences **2011,** 13, (8), 1526-1530.

29. Xiao, L.; Wu, D.; Han, S.; Huang, Y.; Li, S.; He, M.; Zhang, F.; Feng, X. *ACS applied materials & interfaces* **2013,** 5, (9), 3764-3769.

30. Huang, J.; Xie, Y.; Li, B.; Liu, Y.; Qian, Y.; Zhang, S. *Advanced Materials* **2000,** 12, (11), 808-811.

31. Wei, W.; Zhang, C.; Ding, S.; Qu, X.; Liu, J.; Yang, Z. *Colloid and Polymer Science* **2008,** 286, (8-9), 881-888.

32. Lou, X. W.; Wang, Y.; Yuan, C.; Lee, J. Y.; Archer, L. A. *Advanced Materials* **2006,** 18, (17), 2325-2329.

33. Larcher, D.; Bonnin, D.; Cortes, R.; Rivals, I.; Personnaz, L.; Tarascon, J.-M. *Journal of The Electrochemical Society* **2003,** 150, (12), A1643-A1650.

34. Larcher, D.; Masquelier, C.; Bonnin, D.; Chabre, Y.; Masson, V.; Leriche, J.-B.; Tarascon, J.-M. *Journal of The Electrochemical Society* **2003,** 150, (1), A133-A139.

35. Wu, X.-L.; Guo, Y.-G.; Wan, L.-J.; Hu, C.-W. *The Journal of Physical Chemistry C* **2008,** 112, (43), 16824-16829.

36. Wu, H.; Chan, G.; Choi, J. W.; Yao, Y.; McDowell, M. T.; Lee, S. W.; Jackson, A.; Yang, Y.; Hu, L.; Cui, Y. *Nature nanotechnology* **2012,** 7, (5), 310-315.